

Experimental and Numerical Simulation Research on Controllable Shock Wave-Induced Shale Fracturing under Repeated Action

Jianghui Ding, Meijuan Liu,* Yang Zhang, Xun Sun, Qinghe Niu,* Wen Wang, Wei Wang, Yongxiang Zheng, and Chao Yin



Cite This: *ACS Omega* 2024, 9, 13252–13261



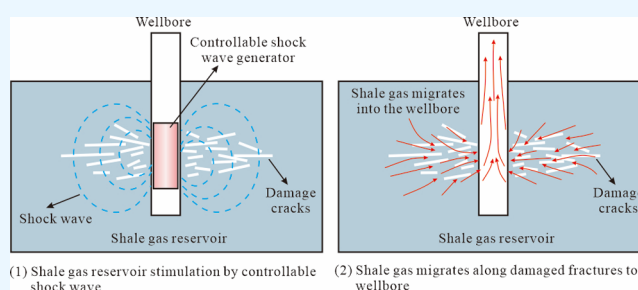
Read Online

ACCESS |

Metrics & More

Article Recommendations

ABSTRACT: Low permeability is a key geological factor constraining the development of shale gas, and reservoir modification to improve its permeability is a prerequisite. Controlled shock wave fracturing can induce the formation of complex fractures in reservoirs and is expected to become an important means of reservoir modification. However, the mechanism of controlled shock wave fracturing in shale and the geological engineering control factors are unclear. Therefore, this article reveals the mechanism and effect of shock wave modification through small-scale experiments and large-scale numerical simulations. Results show that as the impact number increases, a significant increase in large fractures and fracture connectivity within the shale samples is observed, while the correlation between the geometric parameters of the fractures and the number of impacts is weak. High-energy input in the model will cause a larger range of damage to the rock, accompanied by a smaller attenuation index, indicating that the speed of energy attenuation plays a decisive role in rock damage. The influence of crustal stress is greater than the speed of energy attenuation, and higher crustal stress will inhibit the formation of fractures. A moderate increase in the number of controllable shock waves is beneficial for the fracturing effect; however, further increasing the loading number of controllable shock waves will weaken the strengthening effect of the fracturing effect.



1. INTRODUCTION

Currently, the primary energy source worldwide relies mainly on fossil energy, especially in China, where fossil energy accounts for only about 15% of primary energy consumption.^{1–3} In the future economic and industrial development, fossil energy will continue to play a crucial role.^{4–8} Shale gas is an important unconventional natural gas, with China's shale gas reserves reaching nearly 30 trillion cubic meters, ranking first in the world and being very abundant.^{9–11} However, the low porosity and permeability of China's shale gas reservoirs have led to significant development challenges, becoming a key constraint on increasing shale gas production in the country.^{12,13} Therefore, a certain degree of reservoir stimulation is necessary to promote the high-yield and efficient development of shale gas.^{14–19}

Reservoir stimulation can be roughly divided into chemical transformation and physical transformation.^{20–23} Chemical transformation refers to the use of injected solutions to react with the reservoir to increase its permeability.^{24,25} This process is limited by the mineral composition of the reservoir when it is applied on-site. On the other hand, physical stimulation involves applying pressure to induce damage and fractures in the reservoir, thereby increasing its permeability.²⁶ This

pressure can be either static or dynamic.^{27,28} For instance, hydraulic fracturing, as a representative of static methods,²⁹ applies high-pressure water flow to the reservoir to create large fractures along the maximum principal stress direction,^{30–32} gathering oil and gas within a hundred-meter range.³³ Hydraulic fracturing creates large and singular fractures, which can enhance the permeability of the reservoir,^{34–36} yet it remains unfavorable for extensive permeation of gas.^{37,38} Additionally, hydraulic fracturing is associated with long construction periods, high resource consumption, and environmental pollution.^{39,40} For a long time, measures such as high-energy gas fracturing and deep hole presplitting blasting have been taken to increase reservoir permeability through dynamic shock wave methods,^{41–43} which can promote the generation of more small fractures and are more conducive to the large-scale migration of reservoir fluids. However, these methods

Received: December 14, 2023

Revised: February 21, 2024

Accepted: February 27, 2024

Published: March 7, 2024



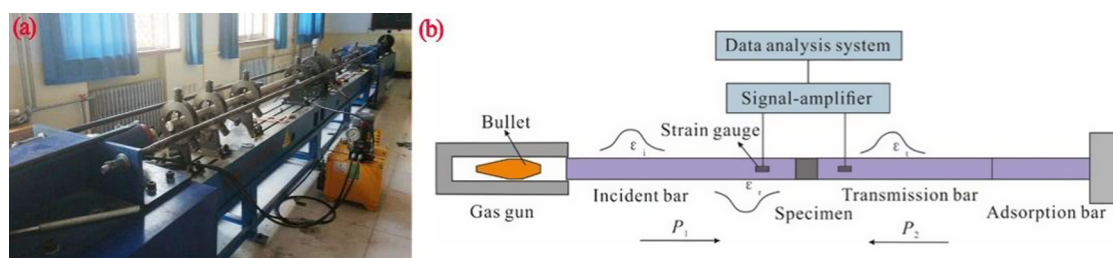


Figure 1. Physical diagram (a) and schematic diagram (b) of the split Hopkinson pressure bar device. (Photograph courtesy of Wen Wang. Copyright 2024.)

Table 1. Physical and Mechanical Parameters of Shale

density (kg m^{-3})	compressive strength (MPa)	elasticity modulus (GPa)	Poisson's ratio	P-wave velocity (m s^{-1})
2393	98.16	9.93	0.12	3580

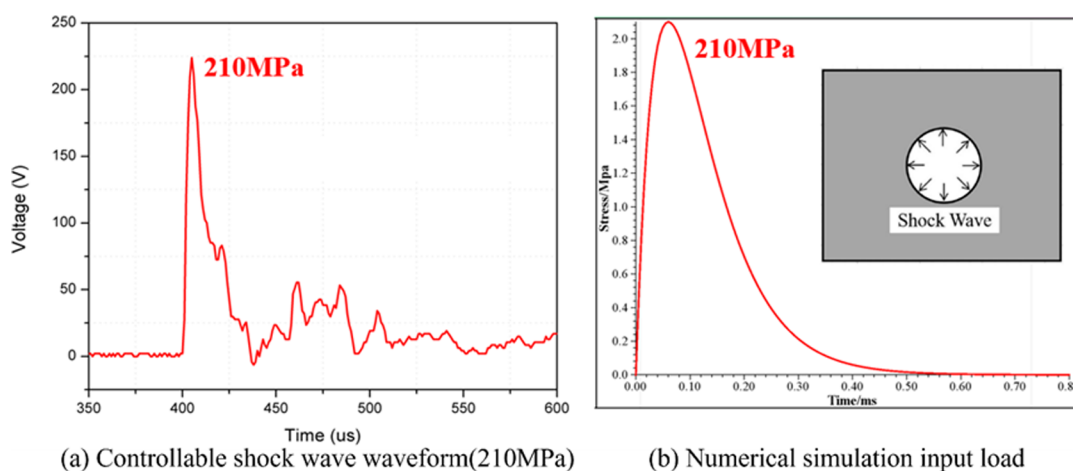


Figure 2. Controllable shock wave and numerical simulation input waveform comparison chart.

have been applied in fields such as coalbed methane extraction^{17,44,17,44} and uranium mine permeability enhancement,⁴⁵ yet they involve intense shock fracturing, which can easily cause wellbore breakage and collapse⁴⁶ and are difficult to implement repeatedly.

Controllable shock wave technology has the advantages of controllable shock waves, repeatability, and simple instrument and equipment operation compared to hydraulic fracturing, high-energy gas fracturing, and blasting-induced fracturing.^{47–50} Zhang et al. have developed an implosion permeation technology based on high-power pulse technology and metal wire electrical explosion,⁵¹ which transforms electrical and chemical energy into the mechanical energy of shock waves. By utilizing the repetitive operation of a pulse power source, controllable and repetitive strong shock waves are generated within a certain area. The single amplitude and impulse of the repetitive shock wave technology are controlled to be below the damage threshold of the wellbore, and the repeated effects can enhance the transformation effect on the reservoir. This method has been verified by other scholars in recent years.^{52,53} Furthermore, corresponding equipment development was carried out, and engineering application of this technology was promoted. For example, the controllable shockwave stimulation technology has been applied in removing blockages and increasing production in oil well reservoirs, and gas extraction of coal mines,^{54,55} indicating that the effect of increasing permeability within a range of tens of meters is

significant. However, Previous research has rarely focused on the field of enhancing shale gas production through controlled shock waves, and studies remain superficial. In particular, there is a lack of in-depth research on the fracturing mechanisms and effects of shale under repeated impacts, which has limited the promotion of this technology in the development of shale gas.

Based on this, the study conducts research on the mechanism of shale gas reservoir stimulation under the repeated action of a controllable shock wave (CSV), using small-scale laboratory experiments and medium-scale numerical simulations. It aims to elucidate the expansion and distribution patterns of shale fractures at the microlevel and reveal the impact mechanism of the number of repetitions on the transformation effectiveness of shale. This research will provide theoretical and technical support for the modification and enhanced development of shale gas reservoirs.

2. EXPERIMENTAL AND NUMERICAL SIMULATION THEORY

2.1. Shock Wave-Induced Fracturing Experiment. The dynamic impact experiment is performed on the split Hopkinson pressure bar device (SHPB) (Figure 1), which is composed of five subsystems, i.e., the drive subsystem, the bar subsystem, the energy absorption subsystem, and the signal acquisition and data processing subsystems. The length of the bullet, incident bar, and transmission bar of the device is 300, 3000, and 2000 mm, respectively, and the diameter of them is

50 mm. They are made of 40Cr alloy steel, with a density of 7810 kg/m³, a longitudinal wave velocity of 5410 m/s, an elastic modulus of 210 GPa, and Poisson's ratio of 0.23. The driving gas pressure in this work was maintained at 16 psi. The direct loading of impact load will produce a rectangular wave in the bar and cause an obvious dispersion effect in the process of signal propagation. A rubber sheet is used to better realize constant strain rate loading. An appropriate amount of Vaseline was used on the end face of the sample to reduce the friction between the sample and the bars. The physical and mechanical parameters of shale are shown in Table 1.

2.2. Determination of Load Curve of Controllable Shock Wave. The measured load curve of the controllable shock wave is shown in Figure 2a. At the moment of detonation, the load of the shock wave rapidly reaches a peak value (210 MPa), and then, the pressure of the shock wave decreases, showing a certain fluctuating trend. Since the amplitude of the shock wave pressure driven by the metal wire and energetic materials is related to the amount of energetic materials, there is no relevant theoretical research to calculate the time-history curve of the pulsed controllable shock wave. This study intends to use the pulse function (eq 1) combined with the experimentally obtained shock wave pressure to determine the shock wave load curve input during numerical simulation.

$$P_t = P_x \zeta [e^{-\alpha t} - e^{-\beta t}] \quad (1)$$

where P_t represents the pressure value acting on the bore wall at time t ; P_x represents the amplitude pressure on the bore wall; α and β are the constants; for the convenience of representing the rising and falling stages, α and β are expressed using eqs 2 and 3:

$$t_r = \frac{1}{\beta - \alpha} \ln\left(\frac{\beta}{\alpha}\right) \quad (2)$$

$$\zeta = \frac{1}{e^{-\alpha t_r} - e^{-\beta t_r}} \quad (3)$$

where t_r is the rise time, which is the time required for the shock wave to rise to the amplitude pressure. Based on the measured shock wave load curve (amplitude pressure of about 210 MPa, rise time of about 50 μ s), the load-time-history curve substituting for the shock wave can be calculated, as shown in Figure 2b.

2.3. Determination of Constitutive Model. This study uses finite difference method (FDM) software for simulation analysis. The constitutive model adopts the Hoek–Brown strength criterion, which is a recognized criterion for describing the nonlinear failure of rock. The expression is as follows:

$$\sigma_1 = \sigma_3 + \sigma_{ci} \left(m_b \frac{\sigma_3}{\sigma_{ci}} + s \right)^\alpha \quad (4)$$

where σ_1 and σ_3 are the maximum and minimum principal stresses; σ_{ci} is the uniaxial compressive strength of the rock; m_b is a decreased value of the material constant m_i , which can be expressed as:

$$m_b = \exp\left(\frac{\text{GSI} - 100}{28 - 14D}\right) m_i \quad (5)$$

where s and α are material constants of the rock:

$$s = \exp\left(\frac{\text{GSI} - 100}{9 - 3D}\right) \quad (6)$$

$$\alpha = 0.5 + \frac{1}{6}(e^{-\text{GSI}/15} - e^{-20/3}) \quad (7)$$

where GSI is the geological strength index, with a range of 5 to 100 (larger values indicate more intact rock); D is the disturbance factor of the rock mass after being impacted, which is related to the stress state of the rock and has a range of 0 to 1.

2.4. Damage Characterization. Deep-seated rock formations are generally heterogeneous and strong, with numerous microscopic pores and fractures.⁵⁶ Under intense external forces, rocks often fail from pre-existing fractures, leading to the development of new fractures, expansion, and continuous propagation of both old and new fractures until they eventually coalesce. Throughout this complex process, the various properties of the rock are significantly reduced, a phenomenon termed rock damage. Damage variables quantify the degree of internal degradation and mechanical properties of the structure, serving as the premise and foundation for studying the process and evolution mechanism of rock damage. The definition of rock damage variables can be broadly categorized into two types: microscopic definition, which primarily focuses on the volume, equivalent area, number, and length of internal microfractures within the rock, and macroscopic definition, which mainly involves defining damage variables from the perspective of rock's elastic modulus, acoustic wave velocity, and unit volume dissipation energy. The methods commonly used to define rock damage include the elastic modulus method, acoustic wave velocity method, unit volume energy dissipation method, crack density method, and strength loss method.

Based on the numerical simulation method used in this study, the software can identify the dissipation of total energy and plastic energy during the dynamic analysis phase. Therefore, a damage variable D is defined to characterize the rock's failure, as shown in the following:

$$D = 1 - \frac{W_p}{W} \quad (8)$$

where D is the damage factor, with a range from 0 (completely damaged) to 1 (undamaged); W is the input total energy; W_p is the energy dissipated by the shock wave as it performs plastic work in the rock.

2.5. Establishment of the Physical Model. According to the on-site test conditions, the actual size of the specimen is 2 × 2 × 1 m, with an outer diameter of the steel casing of 139.7 mm and an inner diameter of 112 mm. The steel casing is embedded 75 cm into the cast block with a perforation segment length of 34 cm, and the center of the perforation segment is located 50 cm inside the block. The perforation arrangement density is 16 holes/m, with 6 holes evenly distributed, at a phase angle of 60°, with each hole spaced 6.67 cm apart.

Based on the actual conditions, steel casing is added to the borehole using shell structural units, with the following specific parameters: inner diameter of 11.2 cm, outer diameter of 13.997 cm, density of 7850 kg/m³, elastic modulus and Poisson's ratio of 200 GPa and 0.25, respectively, and a thickness of 1.4 cm.

The numerical model is established, as shown in Figure 3. To accelerate the calculation speed while ensuring accuracy,

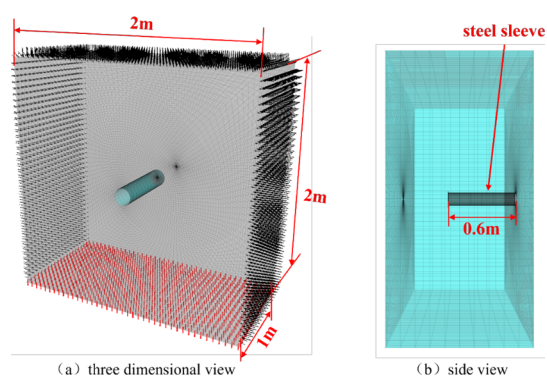


Figure 3. Establishment of physical models.

cylindrical and column shell meshes are used near the center of the borehole, and a radial mesh is used at the model edges, with a total of 162,560 elements. During static calculations, stress boundaries are applied around the perimeter, and the bottom is fixed. During dynamic calculations, viscous boundaries are applied around the perimeter to absorb excessive reflected waves. (In Figure 3a, the red part at the bottom represents the fixed boundary, and the black arrows around it represent the stress boundary. Gray represents viscous boundary conditions.)

2.6. Layout of Monitoring Points. To facilitate the acquisition of the peak stress of the shock wave, stress monitoring points are uniformly distributed at different positions in the model (Figure 4), with radii $R_1 = 0.12$ m,

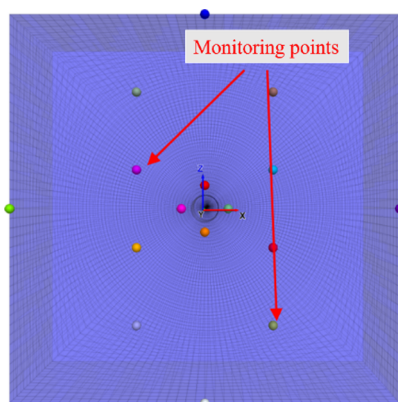


Figure 4. Stress monitoring point layout diagram.

$R_2 = 0.4$ m, $R_3 = 0.7$ m, and $R_4 = 1.0$ m. The coordinates of the monitoring points are listed in Table 2. Therefore, there are 12 monitoring points evenly distributed within the model.

Table 2. Placement of Monitoring Points

radius from center	coordinate			
R_1	(0.12, 0.3, 0)	(0, 0.3, 0.12)	(-0.12, 0.3, 0)	(0, 0.3, -0.12)
R_2	(0.35, 0.3, 0.2)	(0.35, 0.3, -0.2)	(-0.35, 0.3, 0.2)	(-0.35, 0.3, -0.2)
R_3	(0.35, 0.3, 0.6)	(0.35, 0.3, -0.6)	(-0.35, 0.3, 0.6)	(-0.35, 0.3, -0.6)
R_4	(1, 0.3, 0)	(0, 0.3, 1)	(-1, 0.3, 0)	(0, 0.3, -1)

3. ANALYSIS AND DISCUSSION

3.1. Distribution Characteristics of Shale Fractures after Repeated Impacts.

To visually demonstrate the process of shock wave-induced fracturing of shale and achieve three-dimensional visualization of fracture distribution, this study drilled 3 cylindrical shale samples with a diameter of 25 mm and a length of 50 mm. The samples were subjected to shock fracturing experiments at 5 psi for 3, 6, and 9 times. After the experiments, micro-CT scans were conducted, and the fractures were reconstructed in three dimensions by using Avizo software, as shown in Figure 5. It can be seen that the number of shock impacts significantly changed the morphology of the damaged fractures. Under 3 shock impacts, a single continuous large fracture along the bedding was produced. Under 6 shock impacts, multiple continuous and non-continuous fractures along the bedding were generated. Under 9 shock impacts, branching fractures intersecting the bedding fractures were produced, playing a role in connecting the bedding fractures.

The fracture parameters of samples with different numbers of shock impacts are shown in Table 3. Different numbers of shock impacts changed the length, aperture, surface area, and volume of the fractures. Increasing the number of shock impacts can increase the length and aperture of the fractures, but the relationship is not strictly linear. Under the action of impact loads, rock generates damaged fractures, leading to an increase in rock discontinuity. This structure affects the propagation of stress waves, and despite the increasing number of impacts, damage fractures do not continue to develop. On the contrary, the increase in the number of impacts leads to energy accumulation near the load application end, causing the rock structure to become more fragmented and generating more microcracks and porosity. This is also the key reason for the increase in the surface area of pore and fracture structures. However, the volume of the fractures does not show a strictly increasing relationship with the number of shock impacts as it is also related to other geometric parameters. In conclusion, increasing the number of shock impacts is beneficial for generating more pore and fracture structures, but since the permeability of shale is affected by multiple factors, the specific impact of the number of shock impacts on the flow characteristics still needs further study.

3.2. Mechanism of CSV-Induced Cracking in Large-Scale Models. During the controllable shock wave transformation process in shale gas reservoirs, the thickness and burial depth of the reservoir vary,^{57,58} and the effects of the casing and repeated shock wave action make it difficult to predict and evaluate the actual reservoir transformation effect.^{59,60} Therefore, this article focuses on analyzing the following influencing factors: (1) the vertical length of CSV loading, (2) casing, (3) in situ stress, and (4) the number of CSV loadings.

3.2.1. Influence of Vertical Length of CSV Loading on the Fracturing Effect. In this case, no steel casing is installed in the model borehole. The vertical length of the CSV loading represents different input energies, causing differential reservoir fracturing effects (Figures 6 and 7). Figure 6 shows the load applied over the entire borehole, with a length of 60 cm, and Figure 7 shows the load applied according to the actual length (10 cm) of the emission window of CSV.

The different colors in the figure represent different degrees of damage, with the blue area indicating severe damage, the

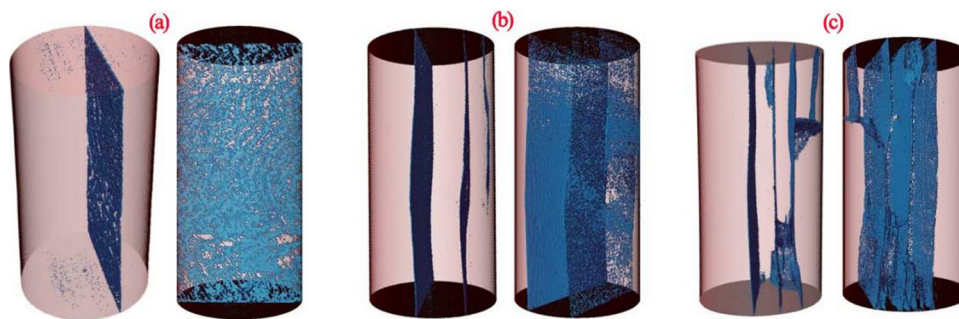


Figure 5. Three-dimensional reconstruction of fractures in samples under different numbers of shock impacts. Sample (a), 3 impacts; sample (b), 6 impacts; and sample (c), 9 impacts.

Table 3. Statistical Table of Damage Frack Parameters (Mean Values)

sample number	length (μm)	aperture (μm)	surface area (μm^2)	volume ($10^8 \mu\text{m}^3$)
Sample (a)	238.706	120.715	0.853	2.53
Sample (b)	410.873	166.701	2.970	1.59
Sample (c)	360.494	150.349	96.902	3.01

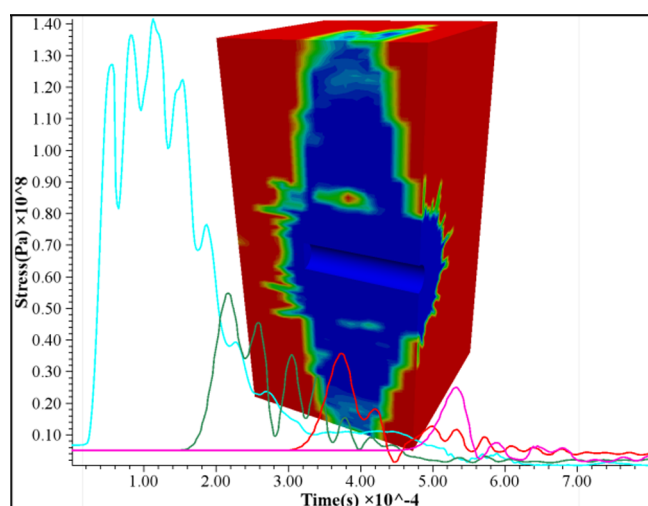


Figure 6. Damage cloud diagram of applied load on the whole blast hole.

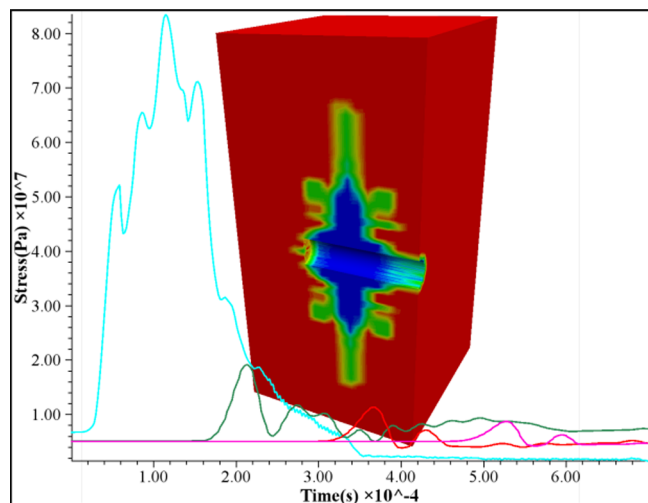


Figure 7. Damage cloud diagram of load applied in the launch window.

green area indicating minor damage, and the red area representing undamaged regions. It is evident that the greater the vertical length of the CSV loading, the larger the extent of damage. The volume of the damaged area in Figure 6 is approximately 4–5 times that in Figure 7. Therefore, increasing the vertical length of the CSV loading can effectively expand the reservoir transformation range, which is very beneficial for enhancing the overall permeability of the shale gas.

The range of rock damage is related to the dissipation of energy. To specifically analyze the relationship between the range of damage and energy dissipation, an exponential function is used to represent the rate of energy decay:

$$P = P_d \bar{r}^{-\alpha} \quad (9)$$

where P is the stress at different positions from the borehole wall, P_d is the incident shock wave intensity, r is the relative distance, $r = R/R_0$, R is the distance from a point to the center of the borehole, R_0 is the radius of the borehole, and α is the decay exponent. A larger decay exponent indicates a faster energy decay.

The distribution pattern of the peak shock wave pressure at different distances is shown in Figure 8. Based on eq 9 and the peak pressure obtained from the model, a fitted formula for shock wave attenuation under the condition of the entire borehole applying load is obtained as $P = 2.1e8\bar{r}^{-0.66}$ (Figure 8a), where the decay exponent is 0.66; and a fitted formula for shock wave attenuation under the condition of load applied at the emission window position is obtained as $P = 2.1e8\bar{r}^{-1.2}$ (Figure 8b), where the decay exponent is 1.2.

This reveals the mechanism of how the vertical length of the CSV loading affects reservoir fracturing. As the vertical length of the CSV loading increases, the attenuation index of the shock wave decreases, allowing it to propagate further and cover a larger area. This is the fundamental reason for the significant differences in the damaged area.

3.2.2. Influence of Steel Casing and Crustal Stress on the Fracturing Effect. In this case, the steel casing is installed in the model borehole, and the different stresses (5 and 10 MPa) are applied around the model to simulate the influence of crustal stress, the damage cloud charts are shown in Figures 9

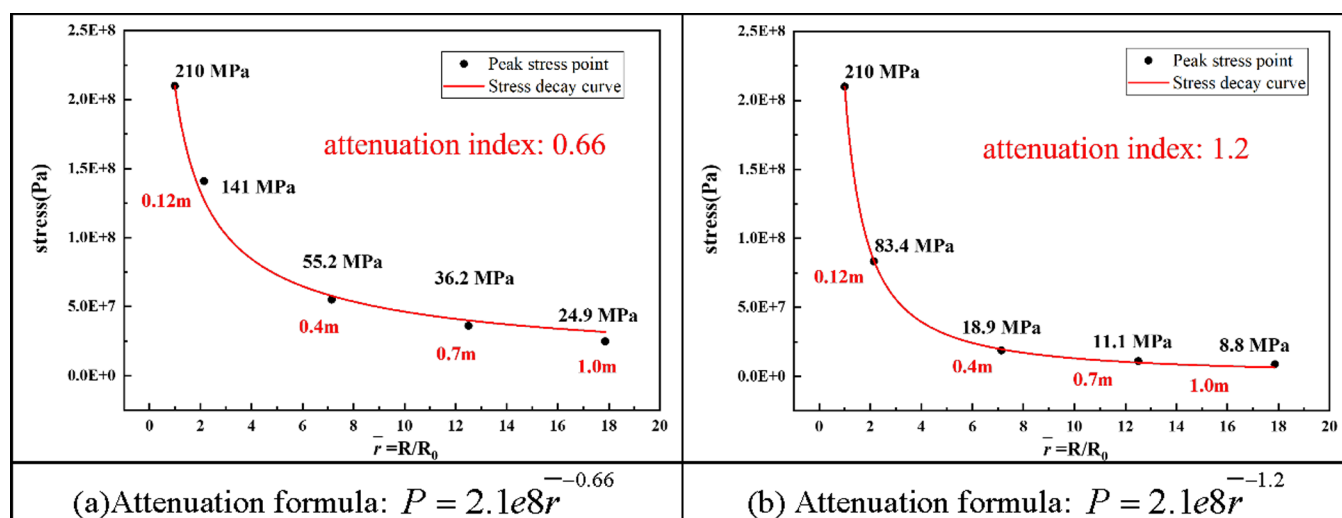


Figure 8. Shock wave attenuation rules under different vertical lengths of CSV loading. (a) Attenuation formula: $P = 2.1e8r^{-0.66}$. (b) Attenuation formula: $P = 2.1e8r^{-1.2}$.

and 10, and the pressure distribution at different monitoring points is shown in Figure 11.

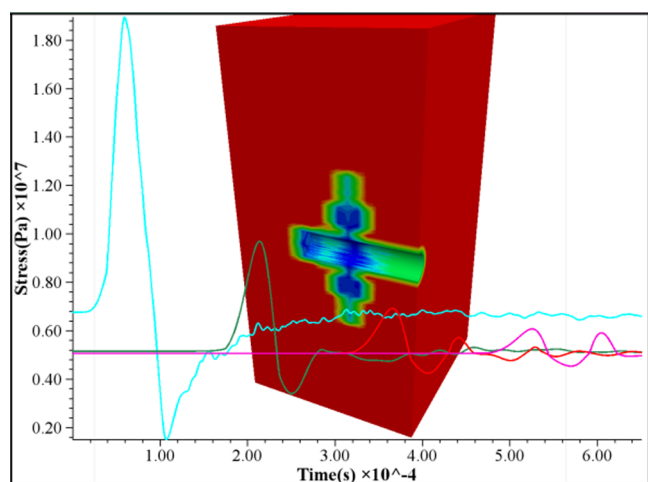


Figure 9. Damage cloud chart under 5 MPa stress condition.

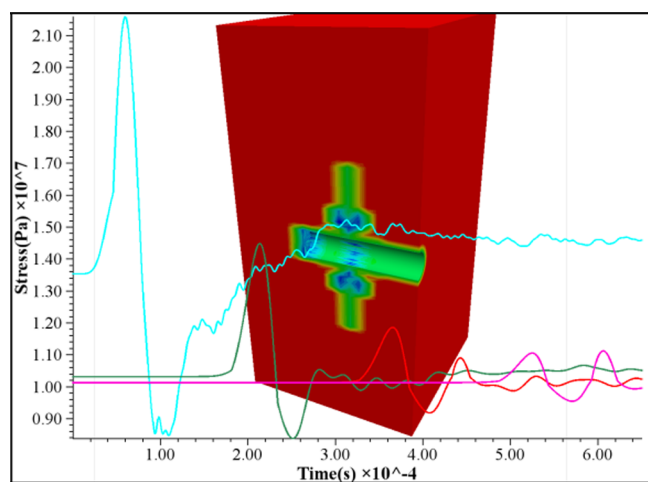


Figure 10. Damage cloud diagram under 10 MPa stress condition.

First, the steel casing significantly impedes the propagation of shock waves, as evidenced by (1) a significant reduction in the damaged area of the rock sample, approximately 20–30% compared to the situation without steel casing and (2) a significant increase in the shock wave attenuation index, approximately 3–5 times higher than without steel casing. This indicates that after the controlled release of shock wave energy, most of it is used to damage the steel casing, with only a small portion used to fracture the reservoir. The inhibitory effect of the steel casing on the shock wave energy is quite significant.

Then, at the 10 MPa stress condition, the peak stress of the shock wave monitoring point should be slightly higher than that under the 5 MPa stress condition. This is because the mechanical strength of the rock increases under high-stress conditions,^{61,62} which is advantageous for the propagation of shock waves. According to the fitting attenuation formula in eq 9, the attenuation index of shock waves at 10 MPa stress conditions is 2.91 (Figure 11b), while the attenuation curve of shock waves at 5 MPa stress conditions is 3.11 (Figure 11a). This indicates that under high-stress conditions, the energy attenuation rate of shock waves is slower than under low-stress conditions. Although high-stress conditions are conducive to the propagation of shock waves, they have a stronger inhibitory effect on the expansion of damaged fractures. Therefore, the controllable impact of shock waves on reservoir damage and fracturing under high-stress conditions is relatively weaker.

Therefore, considering the dual adverse effects of casing and in situ stress, the possible means to maintain a good reservoir stimulation effect is to carry out multiple repeated hydraulic fracturing.

3.2.3. Influence of Number of CSV Loadings on the Fracturing Effect. In this case, the conditions of applying the shock wave once, twice, and three times are considered. The corresponding distribution of plastic zone and damage zone is shown in Figures 12 and 13.

According to Figures 12 and 13, after the first shock wave, no damage zone was found at the model boundary. Based on the stress monitoring results, the shock wave had propagated to the boundary at this point, but the peak pressure had decayed to 11.9 MPa, which is less than the compressive strength of the rock. This can only disturb the rock but has not yet reached the point of fracturing the rock. After the second

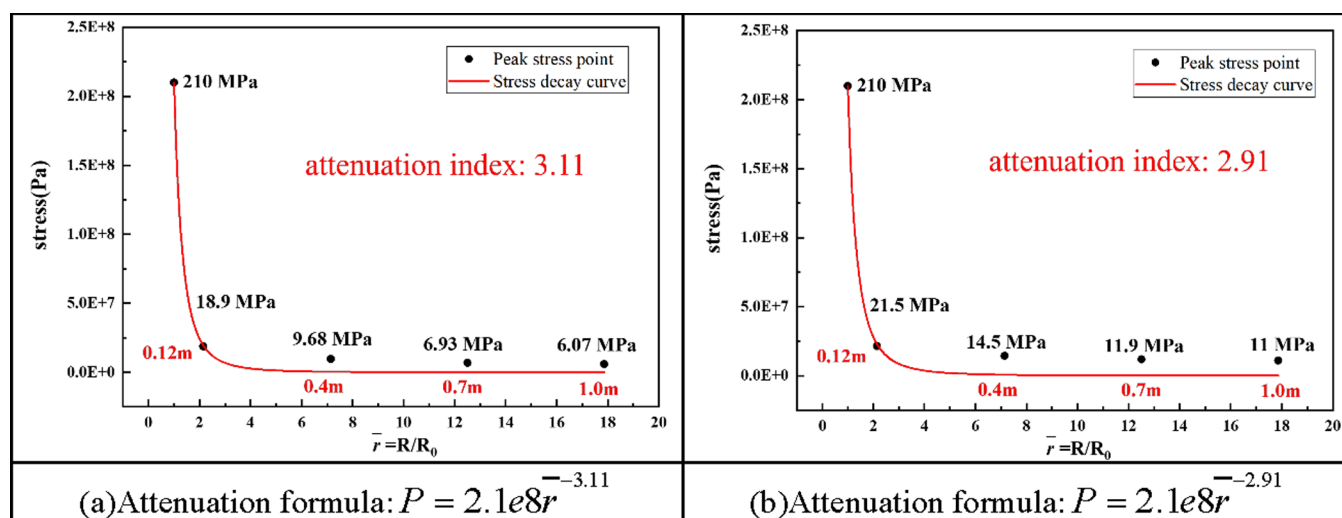


Figure 11. Shock wave attenuation rules under different stress conditions. (a) Attenuation formula: $P = 2.1e8r^{-3.11}$. (b) Attenuation formula: $P = 2.1e8r^{-2.91}$.

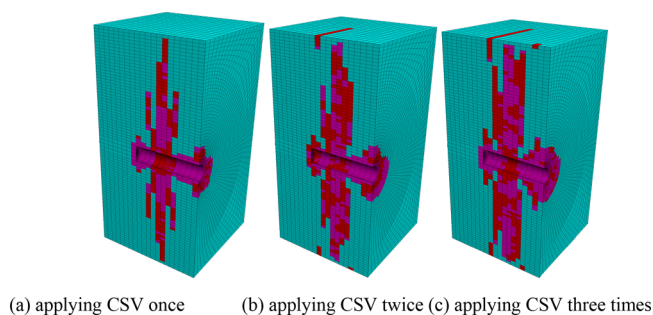


Figure 12. Plastic zone of the sample under different impact times. (a) CSV applied once. (b) CSV applied twice. (c) CSV applied three times.

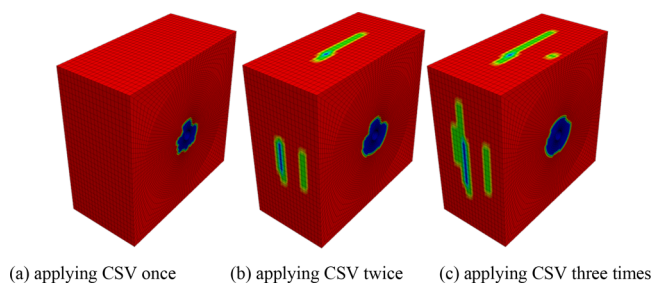


Figure 13. Damage area of sample under different impact times: (a) applying CSV once; (b) applying CSV twice; and (c) applying CSV three times.

shock, the peak pressure at the boundary was 3.58 MPa, which is smaller than the peak pressure from the first shock but damage appeared at the model boundary, indicating that the cumulative damage of the rock played a determining role. After the third shock, the peak pressure at the boundary continued to decrease to 2.6 MPa, and the damage zone continued to expand along the existing fractures. Under multiple shock impacts, due to fatigue damage, the damaged area gradually increased, but no new cracks were formed under repeated shock impacts, only continuing to expand along existing fractures.

Table 4 shows the peak pressures at different distances from the borehole under the action of controlled shock waves three

times, and the attenuation index of the shock waves at different numbers of impacts is calculated according to eq 9. During the first shock, the integrity and strength of the rock are both undamaged, and the shock wave propagates rapidly in the rock, with an attenuation index of 2.9. During the second shock, due to the damage caused by the first shock wave, fractures existed in the rock, and the presence of air due to the rock's noncompactness caused the shock wave to decay rapidly in the air. Therefore, at this time the shock wave energy decayed rapidly, with an attenuation index of 3.8. The attenuation index of the third shock wave was 3.82, which was not much different from the second shock, indicating that although cracks were generated at this time, there were fewer fractures compared to the first two shocks.

In summary, the repeated impacts of shock waves have a positive effect on damage to the rock and help in the expansion of cracks. The main reason for the effect of repeated impacts on the expansion of rock cracks is the cumulative damage of the rock. According to the law of energy attenuation, with an increase in the number of impacts, the shock wave decays more rapidly; thus, the effect of crack expansion in the rock gradually weakens with an increase in the number of impacts.

4. CONCLUSIONS

This study is based on controllable shock wave technology to study the crack propagation law of shale under controllable and repeatable shock wave action and combines numerical simulation to explore the attenuation mechanism of shock wave ability under various factors, filling the gap of CSV in the field of shale gas production. The main conclusions are as follows:

- (1) As the impact number increases, a significant increase in the number of large fractures within the shale samples is observed. At higher numbers of shock impacts, more vertical branching fractures can be generated, promoting fracture connectivity. However, the correlation between the geometric parameters of the fractures and the number of shock impacts is not high.
- (2) High-energy input in the model will cause a larger range of damage to the rock, accompanied by a smaller attenuation index, indicating slower energy attenuation,

Table 4. Energy Attenuation Rules of Different Times of Impact

distance from center of blast hole/m	impacted once/MPa	impacted 2 times/MPa	impacted 3 times/MPa
0.056	2.10×10^{08}	2.10×10^{08}	2.10×10^{08}
0.08	5.37×10^{07}	4.07×10^{07}	4.10×10^{07}
0.1	4.67×10^{07}	3.19×10^{07}	3.14×10^{07}
0.14	3.92×10^{07}	2.58×10^{07}	2.44×10^{07}
0.2	2.43×10^{07}	1.32×10^{07}	1.30×10^{07}
0.4	1.56×10^{07}	8.30×10^{06}	8.42×10^{06}
0.6	1.30×10^{07}	4.46×10^{06}	4.60×10^{06}
0.8	1.19×10^{07}	3.58×10^{06}	2.60×10^{06}
attenuation formula	$P = 2.1e8r^{-2.9}$	$P = 2.1e8r^{-3.8}$	$P = 2.1e8r^{-3.82}$
attenuation index	2.9	3.8	3.82

which shows that the speed of energy attenuation plays a decisive role in rock damage.

- (3) Under the same energy input, increasing crustal stress can slow the attenuation of the shock wave. However, at this point, the influence of crustal stress is greater than the speed of energy attenuation, and higher crustal stress will inhibit the formation of fractures.
- (4) Under multiple shock impacts, the speed of energy attenuation has a less significant impact on the fractures, and the cumulative fatigue effect of multiple impacts contributes to the expansion of fractures. The incremental expansion of rock fractures gradually weakens with an increasing number of shock impacts.

AUTHOR INFORMATION

Corresponding Authors

Meijuan Liu – State Key Laboratory of Electrical Insulation and Power Equipment, Xi'an Jiaotong University, Xi'an, Shaanxi 710049, China; Email: lmj_gt@126.com

Qinghe Niu – Hebei Technology and Innovation Center on Safe and Efficient Mining of Metal Mines, Shijiazhuang 050043, China; State Key Laboratory of Mechanical Behavior and System Safety of Traffic Engineering Structures, Shijiazhuang Tiedao University, Shijiazhuang 050043, China; orcid.org/0000-0001-5695-8355; Email: qingniu@163.com

Authors

Jianghui Ding – CNPC Engineering Technology Research and Development Company Limited, Beijing 102206, China

Yang Zhang – CNPC Engineering Technology Research and Development Company Limited, Beijing 102206, China

Xun Sun – CNPC Engineering Technology Research and Development Company Limited, Beijing 102206, China

Wen Wang – Hebei Technology and Innovation Center on Safe and Efficient Mining of Metal Mines, Shijiazhuang 050043, China; State Key Laboratory of Mechanical Behavior and System Safety of Traffic Engineering Structures, Shijiazhuang Tiedao University, Shijiazhuang 050043, China

Wei Wang – Hebei Technology and Innovation Center on Safe and Efficient Mining of Metal Mines, Shijiazhuang 050043, China; State Key Laboratory of Mechanical Behavior and System Safety of Traffic Engineering Structures, Shijiazhuang Tiedao University, Shijiazhuang 050043, China

Yongxiang Zheng – Hebei Technology and Innovation Center on Safe and Efficient Mining of Metal Mines, Shijiazhuang 050043, China; State Key Laboratory of Mechanical Behavior and System Safety of Traffic Engineering Structures,

Shijiazhuang Tiedao University, Shijiazhuang 050043, China

Chao Yin – Hebei Technology and Innovation Center on Safe and Efficient Mining of Metal Mines, Shijiazhuang 050043, China; State Key Laboratory of Mechanical Behavior and System Safety of Traffic Engineering Structures, Shijiazhuang Tiedao University, Shijiazhuang 050043, China

Complete contact information is available at:

<https://pubs.acs.org/10.1021/acsomega.3c09992>

Notes

The authors declare no competing financial interest.

ACKNOWLEDGMENTS

This study was funded by the Hebei Natural Science Foundation (E2021210072).

REFERENCES

- (1) Zhou, N.; Price, L.; Yande, D.; Creyts, J.; Khanna, N.; Fridley, D.; Lu, H.; Feng, W.; Liu, X.; Hasanbeigi, A.; Tian, Z.; Yang, H.; Bai, Q.; Zhu, Y.; Xiong, H.; Zhang, J.; Chrisman, K.; Agenbroad, J.; Ke, Y.; Mcintosh, R.; Mullaney, D.; Stranger, C.; Wanless, E.; Wetzel, D.; Yee, C.; Franconi, E. A roadmap for China to peak carbon dioxide emissions and achieve a 20% share of non-fossil fuels in primary energy by 2030. *Appl. Energy* **2019**, *239*, 793–819.
- (2) Niu, Q.; Pan, J.; Jin, Y.; Wang, H.; Li, M.; Ji, Z.; Wang, K.; Wang, Z. Fractal study of adsorption-pores in pulverized coals with various metamorphism degrees using N₂ adsorption, X-ray scattering and image analysis methods. *J. Pet. Sci. Eng.* **2019**, *176*, 584–593.
- (3) Ji, Z.; Chen, Z.; Pan, J.; Niu, Q. A novel method for estimating methane emissions from underground coal mines: The Yanma coal mine, China. *Atmos. Environ.* **2017**, *170*, 96–107.
- (4) Xiao, Q.; Wang, Z.; Yang, Z.; Xiang, Z.; Liu, Z.; Yang, W. Novel method for determining the lower producing limits of pore-throat radius and permeability in tight oil reservoirs. *Energy Rep.* **2021**, *7*, 1651–1656.
- (5) Xiao, Q.; Yang, Z.; Wang, Z.; Qi, Z.; Wang, X.; Xiong, S. A full-scale characterization method and application for pore-throat radius distribution in tight oil reservoirs. *J. Pet. Sci. Eng.* **2020**, *187*, No. 106857.
- (6) Niu, Q.; Cao, L.; Sang, S.; Wang, W.; Zhou, X.; Yuan, W.; Ji, Z.; Chang, J.; Li, M. Experimental study on the softening effect and mechanism of anthracite with CO₂ injection. *Int. J. Rock Mech. Min. Sci.* **2021**, *138*, No. 104614.
- (7) Niu, Q.; Cao, L.; Sang, S.; Zhou, X.; Wang, Z.; Wu, Z. The adsorption-swelling and permeability characteristics of natural and reconstituted anthracite coals. *Energy* **2017**, *141*, 2206–2217.
- (8) Song, R.; Wang, Y.; Sun, S.; Liu, J. Characterization and microfabrication of natural porous rocks: From micro-CT imaging and digital rock modelling to micro-3D-printed rock analogs. *J. Pet. Sci. Eng.* **2021**, *205*, No. 108827.

- (9) Gao, S.; Dong, D.; Tao, K.; Guo, W.; Li, X.; Zhang, S. Experiences and lessons learned from China's shale gas development: 2005–2019. *J. Nat. Gas Sci. Eng.* **2021**, *85*, No. 103648.
- (10) Wu, K. China's energy security: Oil and gas. *Energy Policy* **2014**, *73*, 4–11.
- (11) Ren, J.; Niu, Q.; Wang, Z.; Wang, W.; Yuan, W.; Weng, H.; Sun, H.; Li, Y.; Du, Z. CO₂ Adsorption/Desorption, Induced Deformation Behavior, and Permeability Characteristics of Different Rank Coals: Application for CO₂-Enhanced Coalbed Methane Recovery. *Energy Fuels* **2022**, *36* (11), 5709–5722.
- (12) Song, R.; Liu, J.; Cui, M. A new method to reconstruct structured mesh model from micro-computed tomography images of porous media and its application. *Int. J. Heat Mass Transfer* **2017**, *109*, 705–715.
- (13) Song, R.; Wang, Y.; Ishutov, S.; Zambrano-narvaez, G.; Hodder, K. J.; Chalaturnyk, R. J.; Sun, S.; Liu, J.; Gamage, R. P. A Comprehensive Experimental Study on Mechanical Behavior, Microstructure and Transport Properties of 3D-printed Rock Analogs. *Rock Mech. Rock Eng.* **2020**, *53* (12), 5745–5765.
- (14) Ren, L.; Lin, R.; Zhao, J.; Rasouli, V.; Zhao, J.; Yang, H. Stimulated reservoir volume estimation for shale gas fracturing: Mechanism and modeling approach. *J. Pet. Sci. Eng.* **2018**, *166*, 290–304.
- (15) Niu, Q.; Cao, L.; Sang, S.; Wang, W.; Yuan, W.; Chang, J.; Jia, X.; Zheng, W.; Zhang, Z. A small-scale experimental study of CO₂ enhanced injectivity methods of the high-rank coal. *Pet. Sci.* **2021**, *18* (5), 1427–1440.
- (16) Niu, Q.; Wang, Q.; Wang, W.; Chang, J.; Chen, M.; Wang, H.; Cai, N.; Fan, L. Responses of multi-scale microstructures, physical-mechanical and hydraulic characteristics of roof rocks caused by the supercritical CO₂-water-rock reaction. *Energy* **2022**, *238*, No. 121727.
- (17) Niu, Q.; Cao, L.; Sang, S.; Zhou, X.; Liu, S. Experimental study of permeability changes and its influencing factors with CO₂ injection in coal. *J. Nat. Gas Sci. Eng.* **2019**, *61*, 215–225.
- (18) Niu, Q.; Wang, W.; Liang, J.; Yuan, W.; Wen, L.; Chang, J.; Ji, Z.; Zhou, H.; Wang, Z.; Jia, X. Investigation of the CO₂ Flooding Behavior and Its Collaborative Controlling Factors. *Energy Fuels* **2020**, *34* (9), 11194–11209.
- (19) Song, R.; Liu, J.; Yang, C.; Sun, S. Study on the multiphase heat and mass transfer mechanism in the dissociation of methane hydrate in reconstructed real-shape porous sediments. *Energy* **2022**, *254*, No. 124421.
- (20) Niu, Q.; Ma, K.; Wang, W.; Pan, J.; Wang, Q.; Du, Z.; Wang, Z.; Yuan, W.; Zheng, Y.; Shangguan, S.; Qi, X.; Pan, M.; Ji, Z. Multifactor analysis of heat extraction performance of coaxial heat exchanger applied to hot dry rock resources exploration: A case study in matouying uplift. *Tangshan, China, Energy* **2023**, *282*, No. 128277.
- (21) Zhou, X.; Sang, S.; Niu, Q.; Zhang, K.; Liu, F.; Wang, W.; Chang, J. Changes of Multiscale Surface Morphology and Pore Structure of Mudstone Associated with Supercritical CO₂-Water Exposure at Different Times. *Energy Fuels* **2021**, *35* (5), 4212–4223.
- (22) Zhou, X.; Wang, W.; Niu, Q.; Wang, Q.; Su, X.; Zhou, G.; Zhao, L.; Ji, Z.; Qi, X.; Tian, L. Geochemical reactions altering the mineralogical and multiscale pore characteristics of uranium-bearing reservoirs during CO₂+ O₂ in situ leaching. *Front. Earth Sci.* **2023**, *10*, No. 1094880.
- (23) Fu, C.; Du, Y.; Song, W.; Sang, S.; Pan, Z.; Wang, N. Application of automated mineralogy in petroleum geology and development and CO₂ sequestration: A review. *Mar. Pet. Geol.* **2023**, *151*, No. 106206.
- (24) Wang, H.; Cheng, X.; Tian, J.; Li, T.; Wang, W.; Pan, J.; Niu, Q.; Feng, S.; Hao, H.; Zhang, Y. Permeability enhancement of low rank coal through acidization using H₂S solution: An experimental study in the Kuqa-Bay Coalfield, Xinjiang, China. *J. Pet. Sci. Eng.* **2020**, *185*, No. 106476.
- (25) Niu, Q.; Hu, M.; He, J.; Zhang, B.; Su, X.; Zhao, L.; Pan, J.; Wang, Z.; Du, Z.; Wei, Y. The chemical damage of sandstone after sulfuric acid-rock reactions with different duration times and its influence on the impact mechanical behaviour. *Heliyon* **2023**, *9* (12), No. e22346, DOI: 10.1016/j.heliyon.2023.e22346.
- (26) Niu, Q.; Cao, L.; Sang, S.; Zhou, X.; Wang, Z. Anisotropic Adsorption Swelling and Permeability Characteristics with Injecting CO₂ in Coal. *Energy Fuels* **2018**, *32* (2), 1979–1991.
- (27) Wang, W.; Liang, X.; Niu, Q.; Wang, Q.; Zhuo, J.; Su, X.; Zhou, G.; Zhao, L.; Yuan, W.; Chang, J.; Zheng, Y.; Pan, J.; Wang, Z.; Ji, Z. Reformability evaluation of blasting-enhanced permeability in situ leaching mining of low-permeability sandstone-type uranium deposits. *Nucl. Eng. Technol.* **2023**, *55* (8), 2773–2784.
- (28) Chen, Z.; Yuan, Y.; Wang, W.; Zhu, C.; Qin, Z.; Yan, C. Pressure relief and permeability enhancement with carbon dioxide phase transition blasting: fracture, seepage, and practice. *Lithosphere* **2021**, *2021* (Special 4), No. 4983754.
- (29) Yan, C.; Zheng, H.; Sun, G.; Ge, X. Combined finite-discrete element method for simulation of hydraulic fracturing. *Rock Mech. Rock Eng.* **2016**, *49*, 1389–1410.
- (30) Cai, M. Influence of intermediate principal stress on rock fracturing and strength near excavation boundaries—Insight from numerical modeling. *Int. J. Rock Mech. Min. Sci.* **2008**, *45* (5), 763–772.
- (31) Liu, Y.; Zheng, X.; Peng, X.; Zhang, Y.; Chen, H.; He, J. Influence of natural fractures on propagation of hydraulic fractures in tight reservoirs during hydraulic fracturing. *Mar. Pet. Geol.* **2022**, *138*, No. 105505.
- (32) Niu, Q.; Cao, L.; Sang, S.; Zhou, X.; Wang, W.; Yuan, W.; Ji, Z.; Wang, H.; Nie, Y. Study on the anisotropic permeability in different rank coals under influences of supercritical CO₂ adsorption and effective stress and its enlightenment for CO₂ enhance coalbed methane recovery. *Fuel* **2020**, *262*, No. 116515.
- (33) Xiao, Q.; Yang, Y.; Jiang, B.; Zhao, X.; Yu, R.; Liu, Z.; Wang, H. Evaluation method of the micro-occurrence and utilization patterns of gas via a novel method based on nuclear magnetic resonance. *J. Nat. Gas Sci. Eng.* **2021**, *86*, No. 103721.
- (34) Huang, L.; Tan, J.; Fu, H.; Liu, J.; Chen, X.; Liao, X.; Wang, X.; Wang, C. The non-plane initiation and propagation mechanism of multiple hydraulic fractures in tight reservoirs considering stress shadow effects. *Eng. Fract. Mech.* **2023**, *292*, No. 109570.
- (35) Huang, L.; Liu, J.; Zhang, F.; Dontsov, E.; Damjanac, B. Exploring the influence of rock inherent heterogeneity and grain size on hydraulic fracturing using discrete element modeling. *Int. J. Solids Struct.* **2019**, *176–177*, 207–220.
- (36) Yan, C.; Xie, X.; Ren, Y.; Ke, W.; Wang, G. A FDEM-based 2D coupled thermal-hydro-mechanical model for multiphysical simulation of rock fracturing. *Int. J. Rock Mech. Min. Sci.* **2022**, *149*, No. 104964.
- (37) Li, Q.; Qian, Y.; Hu, Q.; Jiang, Z.; Xu, Y.; Shang, X.; Ling, F.; Liu, R.; Li, W. Acoustic Emission Response Mechanism of Hydraulic Fracturing in Different Coal and Rock: A Laboratory Study. *Rock Mech. Rock Eng.* **2022**, *55* (8), 4657–4672.
- (38) Huang, L.; Dontsov, E.; Fu, H.; Lei, Y.; Weng, D.; Zhang, F. Hydraulic fracture height growth in layered rocks: Perspective from DEM simulation of different propagation regimes. *Int. J. Solids Struct.* **2022**, *238*, No. 111395.
- (39) Gao, C.; Cheng, S.; Wang, M.; Wu, W.; Gao, Z.; Li, S.; Meng, X.; Tan, P. Optimization of Carbon Dioxide Foam Fracturing Technology for Shale Gas Reservoir. *Geofluids* **2023**, *2023*, No. 6187764.
- (40) Tao, Z.; Liu, C.; He, Q.; Chang, H.; Ma, J. Detection and treatment of organic matters in hydraulic fracturing wastewater from shale gas extraction: A critical review. *Sci. Total Environ.* **2022**, *824*, No. 153887.
- (41) Hou, B.; Cui, Z. Vertical fracture propagation behavior upon supercritical carbon dioxide fracturing of multiple layers. *Eng. Fract. Mech.* **2023**, *277*, No. 108913.
- (42) Wang, J.; Guo, T.; Chen, M.; Qu, Z.; Liu, X.; Wang, X. Numerical simulation of deflagration fracturing in shale gas reservoirs considering the effect of stress wave impact and gas drive. *Int. J. Rock Mech. Min. Sci.* **2023**, *170*, No. 105478.

- (43) Liu, J.; Su, M.; Zhang, L.; Liu, Z. Coupling model of stress-damage and its application to static blasting technology. *Energy Explor. Exploit.* **2023**, *41* (2), 497–517.
- (44) Liu, P.; Fan, L.; Li, Q.; Zhong, F. Power ultrasound assisted coalbed methane enhancement recovery: Field application and performance evaluation in underground coal mine. *Fuel* **2022**, *324*, No. 124575.
- (45) Wang, W.; Wang, W.; Yuan, W.; Zhou, G.; Feng, X.; Liang, X. Numerical simulation of the effect of water-decoupling charge blasting on reservoir permeability enhancement. *Geomatics, Natural Hazards and Risk* **2022**, *13* (1), 2356–2384.
- (46) Chen, Z.; Yuan, Y.; Yan, C.; Wang, W.; Qin, Z. A Novel Carbon Dioxide Phase Transition Rock Breaking Technology: Theory and Application of Non-Explosive Blasting. *Processes* **2022**, *10* (11), 2434.
- (47) Han, Z.; Li, D.; Li, X. Dynamic mechanical properties and wave propagation of composite rock-mortar specimens based on SHPB tests. *Int. J. Min. Sci. Technol.* **2022**, *32* (4), 793–806.
- (48) Han, Z.; Li, D.; Zhou, T.; Zhu, Q.; Ranjith, P. G. Experimental study of stress wave propagation and energy characteristics across rock specimens containing cemented mortar joint with various thicknesses. *Int. J. Rock Mech. Min. Sci.* **2020**, *131*, No. 104352.
- (49) Tao, J.; Yang, X.; Li, H.; Zhou, J.; Fan, G.; Lu, G. Effects of in-situ stresses on dynamic rock responses under blast loading. *Mech. Mater.* **2020**, *145*, No. 103374.
- (50) Tao, J.; Yang, X.; Li, H.; Zhou, J.; Qi, S.; Lu, G. Numerical investigation of blast-induced rock fragmentation. *Comput. Geotech.* **2020**, *128*, No. 103846.
- (51) Zhang, Y.; Qiu, A.; Zhou, H.; Liu, Q.; Tang, J.; Liu, M. Research Progress in Electrical Explosion Shockwave Technology for Developing Fossil Energy. *High Voltage Eng.* **2016**, *42* (4), 1009–1017.
- (52) Yong, Q.; Aici, Q.; Yongmin, Z. Experiment and Discovery on Permeability Improved Technology of Coal Reservoir Based on Repeated Strong Pulse Waves of High Energy Accumulation. *Coal Sci. Technol.* **2014**, *42* (6), 1–7.
- (53) Li, H.; Qin, Y.; Zhang, Y.; Shi, Q.; Zhou, X. Experimental study on the effect of strong repetitive pulse shockwave on the pore structure of fat coal. *J. China Coal Soc.* **2015**, *40* (4), 915–921.
- (54) Shigang, A.; Dianfu, C.; Yongmin, Z.; Delei, K.; Yang, L.; Di, Z.; Yang, W. Application of controllable electric pulse wave permeability-enhancing technology in the low-permeability coal seam. *Coal Geol. Explor.* **2020**, *48* (04), 138–145.
- (55) Jinghui, Z.; Wanyou, Y.; Chunfeng, Z.; Ang, L.; Qiong, S. Oil Well Productivity Model Under Controlled Shock Wave. *J. Chongqing Univ. Sci. Technol. (Natural Science Edition)* **2021**, *23* (03), 15–19.
- (56) Niu, Q.; Pan, J.; Cao, L.; Ji, Z.; Wang, H.; Wang, K.; Wang, Z. The evolution and formation mechanisms of closed pores in coal. *Fuel* **2017**, *200*, 555–563.
- (57) Wang, L.; Guo, Y.; Yang, C.; Xiao, J.; Lu, C.; Song, Y. Mechanical characterization of continental shale in Sichuan Basin of China and its potential impact on reservoir stimulation. *J. Nat. Gas Sci. Eng.* **2020**, *79*, No. 103346.
- (58) Ifeobia, C. C.; Ahmad, M. A review on the experimental techniques and applications in the geomechanical evaluation of shale gas reservoirs. *J. Nat. Gas Sci. Eng.* **2020**, *74*, No. 103090.
- (59) Yu, H.; Dahi taleghani, A.; Lian, Z.; Lin, T. On how asymmetric stimulated rock volume in shales may impact casing integrity. *Energy Sci. Eng.* **2020**, *8* (5), 1524–1540.
- (60) Zhu, X.; Feng, C.; Cheng, P. Improving reservoir permeability by electric pulse controllable shock wave. *J. Pet. Explor. Prod. Technol.* **2023**, *13* (7), 1655–1667.
- (61) Zhang, Q. B.; Zhao, J. A review of dynamic experimental techniques and mechanical behaviour of rock materials. *Rock Mech. Rock Eng.* **2014**, *47*, 1411–1478.
- (62) Li, X.; Zhou, Z.; Zhao, F.; Zuo, Y.; Ma, C.; Ye, Z.; Hong, L. Mechanical properties of rock under coupled static-dynamic loads. *J. Rock Mech. Geotech. Eng.* **2009**, *1* (1), 41–47.